Jet Propulsion Laboratory
California Institute of Technology

TECHNOLOGY DEVELOPMENT FOR EXOPLANET MISSONS

Technology Milestone Report:
Vortex Coronagraph Technology

E. Serabyn, G. Ruane, A.J. Riggs, W. Baxter, D. Mawet

23 April 2023

National Aeronautics and Space Administration
Jet Propulsion Laboratory
California Institute of Technology
Pasadena, California

Approval page

Prepared by:

E-SIGNED by Eugene Serabyn
on 2023-05-03 16:57:58 GMT

Dr. Eugene Serabyn
Principle Investigator
Senior Research Scientist
NASA/Jet Propulsion Laboratory
California Institute of Technology

Approved by:

E-SIGNED by Brendan Crill
on 2023-05-03 03:36:48 GMT

Dr. Brendan Crill
Deputy Program Chief Technologist
Exoplanet Exploration Program
NASA/Jet Propulsion Laboratory
California Institute of Technology

E-SIGNED by Nicholas Siegler
on 2023-05-03 03:41:27 GMT

Dr. Nicholas Siegler
Program Chief Technologist
Exoplanet Exploration Program
NASA/Jet Propulsion Laboratory
California Institute of Technology

E-SIGNED by Doug Hudgins
on 2023-05-03 15:24:40 GMT

Dr. Douglas Hudgins
Program Scientist
Exoplanet Exploration Program
Science Mission Directorate
NASA Headquarters

Table of Contents

TDEM Milestone Report:
Broadband light rejection with the optical vortex coronagraph

1. Overview

We report the results of our ROSES Technology Development for Exoplanet Missions (TDEM) project entitled ***Broadband light rejection with the optical vortex coronagraph (14-SAT14-0008)***. Our March 2016 homonymous White Paper specified the milestone objective, success criteria, and methodology for computing the milestone metrics. This report follows the general outline of that white paper, and describes the specific vortex mask used in our final measurements, the optical configuration employed in JPL's Decadal Survey Testbed (DST), the experimental approach, the final measurement suite, and our analysis of the results. The main outcome of our work is that we have experimentally demonstrated an average broadband contrast level of $1.8 \pm 0.1 \times 10^{-9}$ in an optical vortex coronagraph operating in the DST. As the attained contrast is within a factor of two of the part per billion contrast targeted in our white paper, the Exoplanet office has decided to accept the three best contrast levels attained so far to close out this project. We will continue to push toward deeper broadband contrast under TDEM award 17-SAT17-0015.

2. Description of the Technology Milestone

TDEM Technology Milestones are intended to document progress in the development of key technologies for potential space-based missions that would detect and characterize exoplanets, such as the earlier Exo-C [1], Habex [2] and LUVOIR [3] mission concepts, and the 6 m IR/O/UV exoplanet flagship mission suggested by the recent Astro2020 decadal report [4], currently called the Habitable Worlds Observer (HWO). This work focuses specifically on the validation of one key TDEM technology – the optical vortex phase mask. Our previous work under 10-SAT10-0009 had earlier demonstrated monochromatic starlight suppression of 5.0×10^{-10} with an optical vortex coronagraph [5,6]. The follow-on work reported here under *14-SAT14-0008* was therefore aimed at broadband (specifically, 10% bandwidth) starlight suppression with a vortex coronagraph. The target milestone specified in our *14-SAT14-0008* white paper was:

Vortex Milestone 1: Broadband Starlight Suppression with Vortex Masks

Using optical vortex phase masks, demonstrate a calibrated average coronagraph contrast of 1×10^{-9} or better over angular separations of $3\lambda/D$ to $8\lambda/D$ from the input point source, for any 10% bandwidth in the wavelength range 300 –1000 nm, for at least one polarization state.

For these demonstrations, our optical vortex phase masks are installed in the focal plane immediately downstream of the pupil stop, which is located on the first of the two deformable mirrors (DMs) in our DST setup. Angular separations are defined in terms of the wavelength, λ, and the diameter, D, of that pupil stop.

2.1. Relevance for a Future Exoplanet Mission

Development of optical vortex coronagraph technology is intended to advance the readiness of mission concepts for the coronagraphic imaging and spectroscopic observation of exoplanetary systems. The optical vortex coronagraph has the advantages of a small inner working angle (IWA), high transmission, a clear, undistorted off-axis field of view, and compatibility with the layout of the Lyot coronagraph [7-9]. The small IWA capability of the vortex coronagraph allows consideration of a range of telescope sizes, and vortex coronagraphs have been selected either as primary or secondary coronagraphs by both the recent Habex and LUVOIR mission concept studies, as well as by the Astro2020 exoplanet flagship mission concept. The vortex coronagraph is thus of particular relevance to the future HWO mission.

Terrestrial exoplanets are expected to have reflected-light fluxes a factor of $\approx 10^{-10}$ less than the fluxes of their host stars, while reflected-light super-Earths and Jovians can have flux ratios of $\approx 10^{-9}$. To detect such exoplanets, image plane contrasts must be comparable, and this TDEM project's goal was to reach image plane contrasts compatible with such super-Earth and Jovian detections. In the following, we use "contrast" to mean the raw detected image-plane flux ratio between off-axis positions in a point source's point spread function (PSF) and the on-axis peak signal. It is expected that post-processing of coronagraph data will improve detection sensitivities to planets and debris disks by roughly an order of magnitude [10], but that aspect is not addressed by this project; i.e., our contrast refers to the raw (unprocessed) contrast in the dark field.

Our contrast specification relates to the average contrast level in a specified dark field of interest around a laboratory source or host star, which should be applicable to any coronagraph that propagates a field of view on the sky to the instrumental focal plane without optical distortions. Exoplanet imaging missions form a high contrast "dark hole" or "dark field" over working angles spanning $n_i\lambda/D$ to $n_o\lambda/2D$, where $n_i\lambda/D$ corresponds to the inner working angle (IWA), as defined by the science requirements and the wavefront control algorithm, and $n_o\lambda/D$ corresponds to the outer working angle (OWA) of the targeted dark hole, i.e., the outermost radius to which the wave front control algorithm is applied. The earlier TPF-C science requirements were an IWA of $4\lambda/D$ [11], but as smaller values are possible with the vortex coronagraph, we selected $3\lambda/D$ for our IWA in this work. The OWA was chosen as $8\lambda/D$, the same as that used in our earlier monochromatic vortex milestone report. This OWA is not an experimental limitation in any sense, as earlier dark-hole demonstrations and extensive optical modeling and tolerancing had shown that dark-field contrasts for the vortex coronagraph generally improve with distance from the image of the target star. Thus, lowering the average contrast simply by increasing the OWA is without real benefit.

Analysis of contrast in the dark field must necessarily account for the statistical nature of the static and "quasi-static" speckles present. Experimentally, speckles will show a distribution of intensities, from which the average dark-hole contrast and statistical confidence levels can be estimated. Statistical measures of both the average intensity and its variance in the coronagraphic dark field are specified in Section 5 below.

2.2. The Vortex Coronagraph

The operation of an ideal optical vortex coronagraph is described in, e.g., [12-14]. A clear telescope input pupil can be described by a field distribution, $P_i(r)$, of

$$P_i(r) = \begin{cases} 1 & \text{for} \quad r < a \\ 0 & \text{for} \quad r > a, \end{cases} \tag{1}$$

where r is the radial coordinate, and a is the radius of the input aperture. Focusing the light leads, via a Fourier transform, to the usual focal-plane field distribution,

$$E_f(\theta) \propto \frac{J_1(ka\theta)}{ka\theta}, \tag{2}$$

where J_1 is the Bessel function of order 1, k is the wavenumber, and θ is the angular radial offset from the center of the stellar PSF.

Passing this focal plane field distribution through a centered optical vortex phase mask multiplies the field by a phase factor corresponding to an azimuthal phase ramp, i.e., $n\alpha$, where α is the azimuthal angle, and n is the "topological charge" of the vortex (i.e., the number of 2π's of phase the mask generates for one circuit about the center), yielding

$$E_f(\theta, \alpha) \propto e^{in\alpha} \frac{J_1(ka\theta)}{ka\theta}. \tag{3}$$

After the vortex phase mask, the light is recollimated and forms a downstream pupil image. Because of the Fourier transform relationship between focal and pupil planes, the vortex's phase wrap, and the following property of Bessel functions, J_n, of order n,

$$J_n(x) = \int_{-\pi}^{\pi} e^{-i(n\varphi - x\sin(\varphi))}\, d\varphi, \tag{4}$$

the reimaged pupil plane distribution is proportional to [12-14]

$$\int_0^\infty J_n(kr\theta) J_1(ka\theta) d\theta \tag{5}$$

instead of the usual

$$\int_0^\infty J_0(kr\theta) J_1(ka\theta) d\theta. \tag{6}$$

This modest change to the integrand alters the downstream pupil intensity distribution dramatically: instead of the original uniformly illuminated pupil (with all of the light inside the entrance pupil), the light in the downstream pupil is instead all to be found outside of the geometric image of the original pupil (for even n), with zero light inside the original pupil in the ideal case (Fig. 1, top right panel.) Outside the post-vortex pupil, the electric field falls off as rippled power laws, leading to multiple azimuthal rings for n > 2. In the ideal case, the starlight can then be completely blocked by a simple aperture stop in the downstream pupil plane with a radius slightly smaller than the pupil image radius. However, if wavefront aberrations are present, residual light will appear inside the pupil.

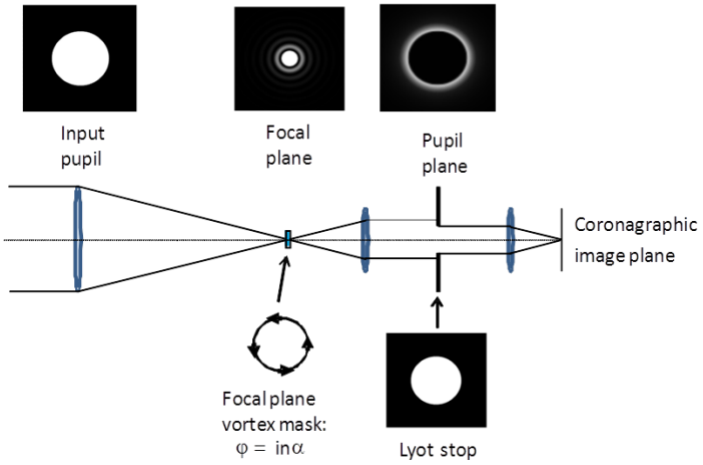

Figure 1. *Layout of the optical vortex coronagraph: an optical vortex phase mask in the focal plane yields a downstream pupil image in which all of the on-axis starlight appears outside of the original pupil's image, where it is blocked by an aperture (Lyot) stop.*

2.3. The Vortex Mask

An ideal vector-vortex phase mask is a planar, spatially-variant diffractive waveplate: it has an achromatic phase shift of half a wave everywhere in the mask plane, but a fast-axis orientation pattern that varies spatially across the mask plane to yield a spatially-variant geometric phase shift in the output beam. The advantages and disadvantages of different ways of implementing optical vortex phase masks are discussed in [15] and for this project we have developed vector vortex phase masks made of liquid crystal polymer (LCP) layers [8,14], due to their manufacturability and applicability to short (i.e., near-infrared, visible and near-ultraviolet) wavelengths. For a spatially-variant LCP fast-axis orientation pattern that rotates azimuthally as $n\alpha/2$, the output geometric phase shifts for the two circular polarization states are given by the desired patterns, $\pm n\alpha$.

Our LCP vortex masks were manufactured by Beam Engineering (Beamco). To achieve an achromatic half-wave phase shift across a 10% spectral band, Beamco relies on a well-known multi-layer achromatization technique (Fig. 2), in which three successive HWP layers are rotated relative to each other by $\approx 60°$ [16]. The mask used here was composed of three such individually-rotated HWP layers, each of which itself is made up of a small number of ~ hundred-nanometer thick sub-layers. Each HWP layer is uniform in the vertical direction (i.e., perpendicular to the vortex plane), but shows a vortex fast-axis orientation pattern in the device plane. The result is a more achromatic HWP in the form of an approximately 1 μm thick LCP slab that is contained between two glass substrates with anti-reflective coatings on the external surfaces, as shown in Fig. 3.

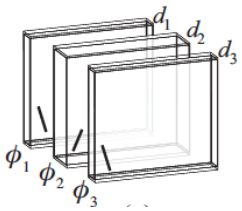

Figure 2. *Classical uniform multilayer approach to broadening waveplate passbands [17]. The three individual optical axis orientations are shown.*

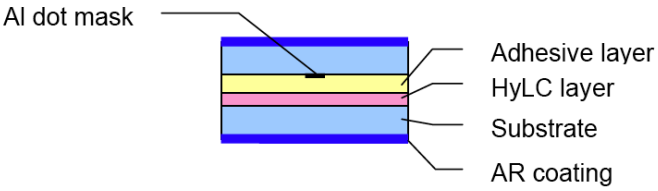

Figure 3. *Cross-section of the sandwich design of the liquid crystal polymer vortex mask. The hybrid liquid crystal polymer (HyLC) layer is situated between two glass disks.*

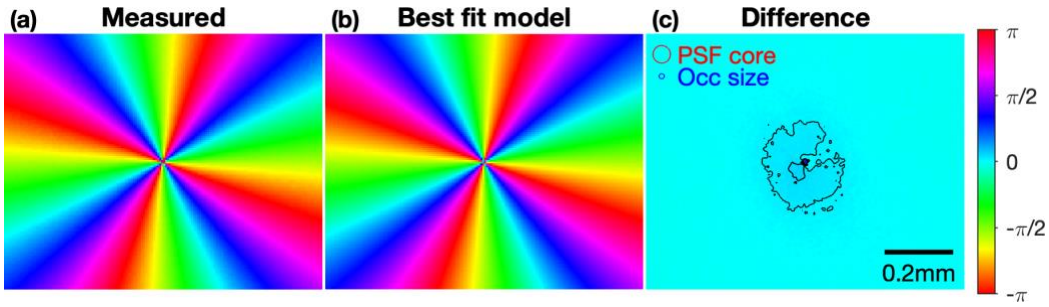

Figure 4. *Vortex mask phase pattern characterization at λ = 650 nm. (a) Geometric phase shift derived from the measured fast axis orientation. (b) The best fit model of the vortex phase pattern. (c) The difference between (a) and (b). The red circle shows the size of the point spread function (PSF) core in the testbed configuration presented below (i.e., an angular radius of 1.22 λ/D corresponding to the first null in the Airy pattern). The contour lines show phase steps of π/40.*

The specific mask that yielded best contrast results in the DST (labelled V650-BW10-Q2-UUU-CDD15-OD7(2)), was received by JPL in Sept. 2020. The mask is a charge 4 vortex mask, designed to be achromatic over a bandwidth of at least $\Delta\lambda/\lambda = 10\%$ centered at 650 nm. The central phase singularity in most masks is blocked by a small metallic circular occulter, but this particular mask had none. The complete set of mask specifications, as ordered, are listed in Table 1.

We first characterized the vortex mask using a Mueller matrix spectro-polarimeter (MMSP; Axometrics Axostep) that measures the full Mueller matrix (MM) for transmitted light at each pixel in a microscope image of the mask at several visible wavelengths, using diffuse transmitted illumination. In our setup, the MM measurements were at wavelengths

of 450-800 nm in sequential steps of 50 nm at a spatial sampling of 5.8 μm per pixel for 128 x160 pixels (or 0.74 x 0.93 mm).

Figure 4a shows the geometric phase shift for one circular polarization, as calculated from the measured orientation of the fast axis at $\lambda = 650$ nm. We fit the expected geometric pattern to the measured pattern to numerically determine the vortex center and azimuthal rotation angle offset (Fig. 4b). As the MMSP cannot distinguish between fast axis orientations differing by π radians, we unwrapped the fast axis angles by adopting the π-offset that gives a phase shift that best matches the vortex pattern at each pixel. We then subtracted the best fit vortex phase pattern to determine the errors in the phase pattern due to fast axis orientation errors (Fig. 4c). We find that the phase error is centrally peaked and slightly asymmetric with a peak of $\sim \pi/10$. The first $\pi/40$ contour occurs at approximately 122 μm from the center and $\pi/20$ is exceeded within the inner southwest lobe at a maximum radius of 52.3 μm.

We also used the MMSP to measure the retardance near the center of the device. Figures 5a-d show the resultant retardance maps at wavelengths of 550, 600, 650, and 700 nm. While an ideal vortex mask would have 180° retardance everywhere for all wavelengths, this mask shows a relatively uniform retardance that is wavelength dependent, with a median retardance error < 2° within a $\Delta\lambda/\lambda = 0.1$ passband centered near 635 nm (Fig. 5e). Table 2 provides the retardance error statistics determined from these MMSP images. In the following, we use $\lambda_0 = 635$ nm as the central wavelength, which is slightly smaller than the design wavelength of $\lambda_d = 650$ nm, to make use of the band with the lowest bulk retardance error. In addition, a cross-like defect is seen near the center of the mask at all wavelengths (indicated by fiducial hash marks) as well as small variations at high spatial frequencies.

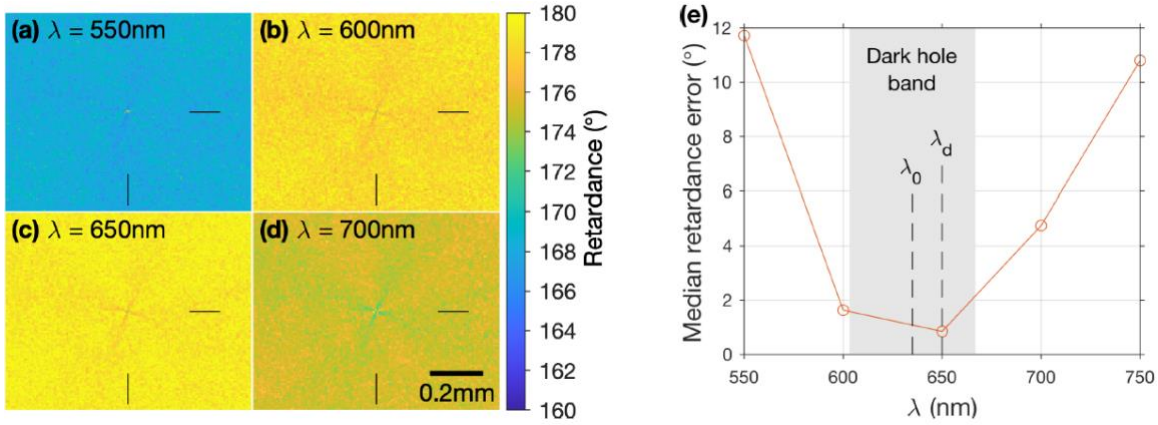

Figure 5. *Focal plane mask retardation measurements. (a)-(d) Retardance maps at wavelengths of (a) 550, (b) 600, (c) 650, and (d) 700 nm. (e) Median retardance error within images shown. The grey area shows the wavelength range used for the testbed results below, with a central wavelength of 635 nm and a bandwidth of 10%. The design central wavelength of the mask was 650 nm.*

Table 1: Vortex Mask Specifications

Quantity:	
Substrate:	
material	Glass index matched to average index of the LCP material Glass must have no birefringence
diameter	1 inch round substrates; diameter not to exceed 1 inch after gluing
thickness	~ 2 – 3 mm; thinner is better, but not required
surface quality	λ/10 requirement; λ/20 rms desirable
Optical properties:	
Center wavelengths	650 nm
Bandwidth	At least 10%, i.e., 617.5 – 682.5 nm
Retardance requirement	180° +/- 1° over the desired 10 % band
Retardance goal	180° +/- 0.1° over the desired 10 % band
Angle of incidence	Normal incidence
AR coating	R < 0.1 % across the 10% band of interest (with 0.01% goal)
Total transmission	≥ 90% within the 10% band of interest
Clear aperture	80-90%
Device structure:	
Vertical structure	AR/substrate/black-dot/adhesive/LCP-layers/substrate/AR
LCP layer structure	3 devices with uniform rotated layers (UUU); 1 device at each of the three central wavelengths specified: 550 nm, 650 nm, and 750 nm
Device q	q = 2 (i.e., LCP fast axis orientation = 2x azimuthal angle)
Central vortex defect diameter	< 5 microns; the smaller the better
Front/back discrimination	Substrates with black dot and vortex layers are to be identified with marks on the sides of their respective substrates
Central opaque dot:	
Central opaque dot diameter	15 microns
Centration of opaque dot	Opaque dot centered over central defect to ~ 1 micron
Central opaque dot quality	No splattering of dot material beyond geometric dot
Central opaque dot transmission	< 10^{-7} if possible

Table 2: Retardance error statistics in Fig. 5.

Wavelength (nm)	Mean retardance (°)	Mean error (°)	RMS error (°)	Std. dev. (°)
550	168.3	-11.7	11.7	0.8
600	178.4	-1.6	1.8	0.8
650	179.1	-0.9	1.1	0.6
700	175.2	-4.8	4.8	0.7

2.4. Testbed configuration

2.4.1. Spectral polarization filtering

To fully understand the testbed configuration, we first describe a technique used to broaden the starlight-rejection passband [18]. As described earlier, a vector vortex is a geometrical structure, i.e., a spatially variant HWP in which the optical axis orientation is a function of position. A vector vortex is thus achromatic to first order by virtue of the geometry of its structure. A perfect HWP flips circular polarization (CP) states, and the vortex's fast-axis orientation pattern yields the phase pattern in the output CP state that redirects the light in that CP state outside of the downstream pupil, where it is rejected by the Lyot stop. However, the real retardance (Fig. 5) is not exactly 180°, which allows a small fraction of the light to leak through the HWP in the original CP state, unaffected by the vortex phase. In the subsequent pupil plane, this light reimages the original pupil, which leads to an Airy pattern in the final image plane. This extra light leakage can be decreased by filtering out (removing) the initial CP state after the Lyot stop. To carry out this "spectral polarization filtering," it is thus necessary to first select (transmit) one of the two CP states upstream of the vortex, and then to reject that CP state at the end (Fig. 6). The DST testbed was therefore configured to enable the selection of a single input CP state, and its rejection at the output end, to enable spectral polarization filtering.

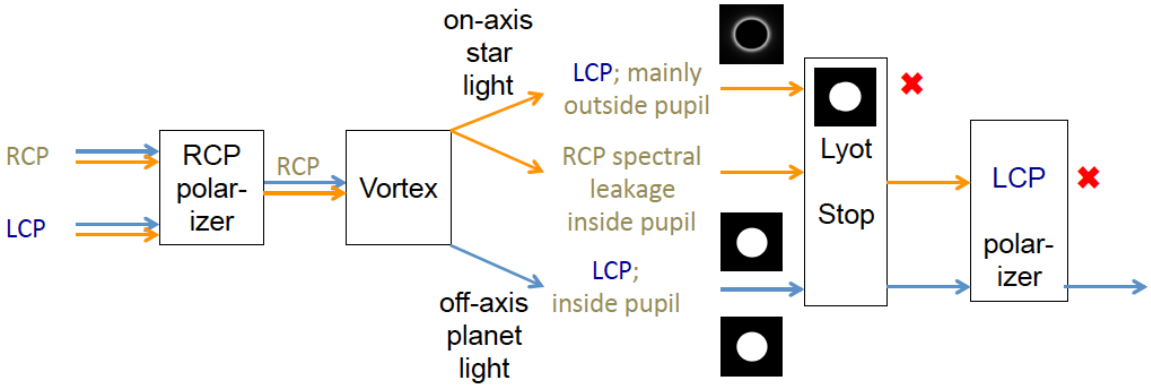

Figure 6. *Spectral polarization filtering. The starlight is shown in orange, and the planet light in blue. RCP and LCP stand for right (left) circular polarization, respectively. The starlight outside the pupil is rejected by the Lyot (aperture) stop, while the spectral starlight leakage inside the pupil is rejected by a circular polarizer.*

2.4.2. The DST. The DST is a coronagraph instrument designed to achieve extremely high contrast (on the order of 10^{-10}) [19]. Figure 7 shows the layout of the DST used for this experiment. To simulate the star, a supercontinuum laser source (NKT SuperK Extreme) is coupled to a photonic crystal fiber (PCF) that passes through the air-to-vacuum interface. A remote-control variable filter (NKT Varia) is used to select the source passband. To generate a single CP state, the light exiting the fiber is collimated by an off-axis parabolic mirror (OAP) and passed through a linear polarizer (LP) and quarter wave plate (QWP) with a 45° relative clocking angle. This light is focused onto a 4 μm diameter pinhole (PH) with an achromatic doublet lens to create a pseudo point source representing a star.

The light from the PH is collimated by a 1.52 m focal length OAP towards the first deformable mirror (DM1) where a circular pupil mask (PM; 46.6 mm diameter) defines the system entrance pupil. The effective resolution is 20.5 μm at a wavelength of 633 nm making this pinhole unresolved (its diameter being 20% of the angular resolution). A second deformable mirror (DM2) is located 1 m downstream of DM1. DM1 and DM2 have 48 x48 actuators based on Lead Magnesium Niobate (PMN) electroceramic arrays with 1 mm pitch manufactured by Northrop Grumman's AOA Xinetics (AOX).

After DM2, a second 1.52 m focal length OAP focuses the light onto the focal plane mask (FPM) with a focal ratio of 32.7. The beam transmits through the FPM and a 761 mm focal length OAP creates an image of the pupil with a diameter of 23.3 mm at the position of the Lyot stop (LS). The LS is a circular aperture with a diameter of 18.6 mm (80% of the geometric pupil diameter). After passing through the Lyot stop, the beam is focused onto a small focal-plane field stop (FS), the purpose of which is to block most of the bright starlight surrounding the desired dark-hole region from reaching the camera plane or accidentally scattering back into the dark hole downstream of the FS plane. The FS is D-shaped, and offset from the star image, so as to allow a "1-sided" dark hole to be generated next to the star. This is done because a single DM cannot correct both amplitude and phase on both sides of the star, and when this project's guiding white paper was written, only a single DM was foreseen. Moreover, even with two DMs, as in the DST, the contrast is a bit better in a 1-sided dark hole. The physical FS actually employed is slightly oversized compared to the desired dark hole extent, with an aperture large enough to accommodate the range of dark hole sizes needed by multiple TDEM projects. Its open aperture is thus a few λ/D larger than our specified dark hole region, the actual size of which is selected in software. After the FS, the light is recollimated by an OAP and passes through the circular analyzer (QWP+LP) and is focused by a final OAP onto the camera (Andor Neo sCMOS).

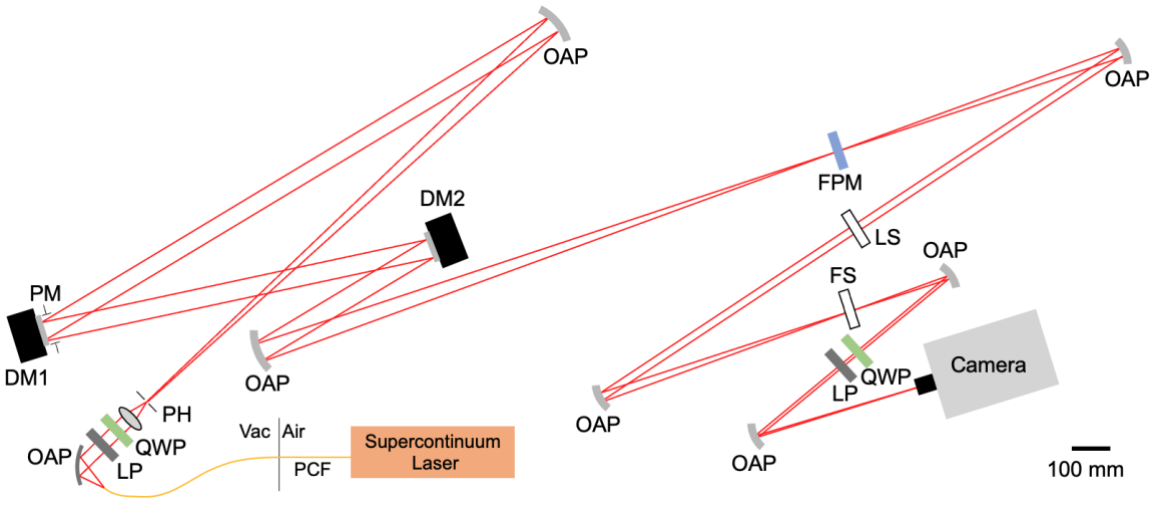

Figure 7. *Schematic of the Decadal Survey Testbed (DST). PCF: Photonic Crystal Fiber. Vac: Vacuum. OAP: Off-axis parabolic mirror. LP: Linear Polarizer. QWP: Quarter-wave plate. PH: Pinhole. PM: Pupil mask. DM: Deformable Mirror. FPM: Focal plane mask. LS: Lyot stop. FS: Field stop.*

2.5. Differences Between Flight and Laboratory Demonstrations

There are several important differences between the laboratory demonstration and flight implementation. Each is addressed briefly here.

Starlight: In a space coronagraph, the spectrum of incident starlight would resemble black body radiation, while here the source was a filtered supercontinuum laser. The laser provides a photon flux that is comparable to or larger than the target stars to be observed. The goal of this milestone was to demonstrate the contrast that can be achieved, without consideration of the source intensity. A bright source is a convenience that does not compromise the integrity of the demonstration, as it affects only integration times.

Unlike the light collected by a telescope from a target star, the intensity of the testbed beam is not completely uniform across the pupil. Typically, this non-uniformity is a center-to-edge "droop" of a few percent, corresponding to the diffraction pattern from the small pinhole. This small level of non-uniformity is expected to have negligible effect on the final contrast, as the wavefront control algorithm accommodates these small effects without the need for improved illumination uniformity.

Spacecraft dynamics: A control system is required in flight to stabilize the light path against motions of the spacecraft. The dominant effects of spacecraft dynamics are jitter of the star image on the coronagraph focal plane mask and beam walk in the optics upstream of the focal plane mask. As a specific example, the ACCESS analysis [20] showed that for fourth-order coronagraphs (including Lyot and vortex coronagraphs) with an inner working angle of $3\lambda/D$, pointing errors need to be less than $\pm$ 0.03 λ/D rms to limit the corresponding contrast degradation to less than 2×10^{-10}. The concept models have shown that the required pointing stability can be achieved in space with current high Technology Readiness Level (TRL) systems. Scaled to the HCIT, this would correspond to an ability to center the vortex mask on the "star" within 1.5 μm, or about 0.2 pixels when projected to the CCD focal plane. The stability of the testbed, including the centration of the star on the vortex, is untraceable to spacecraft dynamics. In practice, the DST often exhibits alignment drifts that are larger than expected in the space environment, but these tend to decrease with time under vacuum. As such we relied on favorable periods of thermal and mechanical stability of the HCIT.

Polarization separation: In the DST, a single input polarization state is selected by the upstream circular polarizer prior to injection into the testbed through the pinhole. This allows wavefront quality to be unaffected by having the circular polarizer in the beam. On the other hand, in flight, the polarizations may need to be split by a free space optic that could affect wavefront quality. The exact flight configuration is not known, but one way to potentially avoid a free-standing quarter wave plate is to combine a planar QWP device with the vortex mask in a single planar focal plane device. Moreover, other types of vortex phase mask, such as the scalar vortex phase mask, may not require polarization splitting. As such, here we begin with a single-polarization dark hole.

3. Computation of the Metric

3.1. Definitions

The "contrast" metric requires measurement of the intensity of the dark-hole speckle field relative to the intensity of the central star. The contrast can be assessed in terms of statistical confidence to capture the impact of experimental noise and uncertainties. Here we define the terms involved and describe the measurements and data products.

3.1.1. "Raw" Image and "Calibrated" Image. Standard techniques for the acquisition of CCD images are used. A "raw" image is defined as the pixel-by-pixel image obtained by reading the charge from each pixel of the CCD, and amplifying and sending it to an analog-to-digital converter. A "calibrated" image is defined as a raw image that has had background bias subtracted. Saturated images are avoided in order to avoid the confusion of CCD blooming and other potential CCD nonlinearities. All raw images are permanently archived and available for later analysis.

3.1.2. "Scratch" is a DM setting in which actuators are set to a predetermined surface figure that is approximately flat (~ 20 volts on each actuator).

3.1.3. Our "star" is a small (4-μm diameter) pinhole illuminated with light relayed via optical fiber from a source outside the HCIT vacuum wall. The pinhole is roughly 20% of Fλ at 633 nm. This "star," the only source of light in the optical path of the HCIT, is a stand-in for the star image that would have been formed by a telescope system.

3.1.4. The "algorithm" is the computer code that takes as input the measured speckle field images, and produces as output a voltage value to be applied to each element of the DM, with the goal of reducing the intensity of speckles.

3.1.5. The "contrast field" is a dimensionless map representing, *for each pixel of the detector*, the ratio, r, of its measured intensity to the value of the peak of the central stellar PSF that is measured in the same testbed conditions (light source, exposure time, Lyot stop, etc.) when the focal plane vortex mask is removed. The calibration of the contrast field is detailed in Sections 3.2 and 3.3.

3.1.6. The "average contrast," c_i, for the ith dark hole in a sequence of dark holes, is a dimensionless quantity that is the average value of the contrast field over the pixels in the dark hole specified i.e.,

$$c_i = \frac{1}{m}\sum_{1}^{m} r_m,$$

where m is the number of pixels in the selected dark hole.

3.1.7. "Statistical Confidence". The interpretation of measured numerical contrast values shall take into consideration, in an appropriate way, the statistics of measurement, including detector read noise, photon counting noise, and dark noise.

The milestone objective is to demonstrate with high confidence that the true contrast value in the dark field, as estimated from our measurements, is equal to or better than the required threshold contrast value C_0. The estimated true contrast value shall be obtained from the average of the set of four or more contrast values measured in a continuous sequence (over an expected period of approximately one hour).

For this milestone the required threshold is a mean contrast value of $C_0 = 1.0 \times 10^{-9}$ with a confidence of 90% or better. Estimation of this statistical confidence level requires an estimation of variances. Given that our speckle fields contain a mix of static and quasi-static speckles (the residual speckle field remaining after the completion of a wavefront sensing and control cycle, together with the effects of alignment drift following the control cycle), as well as other sources of measurement noise including photon detection statistics and CCD read noise, an analytical development of speckle statistics is impractical. Our approach is to compute the confidence coefficients on the assumption of Gaussian statistics. The full set of measurements is also available to enable computation of the confidence levels for other statistics.

At any time in the demonstration, the instantaneous contrast is subject to laboratory conditions, including the quality of the optical components, their alignment, any drift in their alignment over time, and the effectiveness of each wavefront sensing and control cycle. With each iteration, our nulling procedure attempts to improve the contrast value, thus compensating for any drift or changes in alignment that may have occurred since the previous iteration, and further variations may be expected due to experimental noise and any limitations in the algorithm. The data set built up from a sequence of such iterations provides a distribution of contrast values, which will be regarded as Gaussian about a mean contrast for the data set. We therefore consider the mean contrast value as representative of the true contrast value for a data set, and the distribution of contrast determinations among the iterations within the data set as a combination of both random wavefront control errors and random measurement errors. The mean contrast values and confidence limits are computed as follows. The average contrasts, c_i, of each of the last few (n) images in an iteration sequence are then averaged to compute what we call the *mean contrast value*, $\hat{c}$, via

$$\hat{c} = \frac{1}{n}\sum_{i=1}^{n} c_i.$$

(Note that $\hat{c}$ is thus the temporal average of the spatially-averaged dark-hole contrasts.)

The standard deviation σ_{each} in the contrast values c_i obtained for individual images within the set, which includes both the measurement noise and the (assumed random) contrast variations due to changes in the DM settings for each speckle nulling iteration, is:

$$s_{each} = \sqrt{\sum_{i=1}^{n} \frac{(c_i - \hat{c})^2}{n - 1}}$$

The mean contrast estimate $\hat{c}$ is subject to uncertainty in the contrast measurements $\sigma_{mean} = \sigma_{each} / \sqrt{n}$ and the independently-determined photometry error σ_{phot}. With the asumption that the contrast values have a Gaussian distribution about the mean contrast, the statistical confidence that the mean contrast is less than $C_0 = 1 \times 10^{-9}$ is given by:

$$conf = \frac{1}{\sqrt{2\pi}} \int_{-\infty}^{t} e^{-z^2/2} dz$$

where $t = (C_0 - \hat{c}) / s$ *and* $s = \sqrt{s_{mean}^2 + s_{phot}^2}$. The values $\hat{c}$ and σ are the milestone metrics. The 90% confidence value is the value C_0 such that *conf* $(C_0) = 0.9$.

3.2. Measurement of the Star Brightness

The raw contrast is approximated by the "normalized intensity" defined by the stellar intensity normalized to the peak of the unocculted on-axis point spread function, which was measured prior to each wavefront control trial by offsetting the focal plane mask by 1mm (leaving all other optical elements in place) and taking an unsaturated short-exposure image. A typical flux level was ~1e8 photons per second per pixel at the PSF peak, though this changes with wavelength and time due to slow drifts in the system.

3.3. Measurement of the Coronagraph Contrast Field

Each "coronagraph contrast field" is obtained as follows:

3.3.1. The vortex mask is centered on the star image.

3.3.2. An image (typical exposure times for the milestone runs were 2 min) is taken of the coronagraph field (the suppressed star and surrounding speckle field). The dimensions of the target areas, as shown schematically in Figure 8, are a dark (D-shaped) field extending from 3 to 8 λ/D, which is bounded by a straight line that passes 3 λ/D from the star at its closest point, and by a circle of radius 8 λ/D centered on the star.

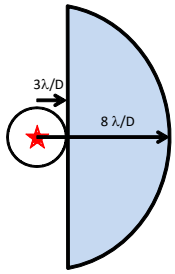

Figure 8. *Target high-contrast dark field from 3 to 8 λ/D, as described in the text. The location of the suppressed central star is indicated in red.*

3.3.3. Each image is normalized to the "star brightness" as defined and described in Section 3.2, i.e., the fixed relationship between peak star brightness and the integrated light in the speckle field outside the central DM-controlled area was used to estimate the star brightness associated with each coronagraph image.

3.3.4. The mean contrast is the sum of all pixel contrast values in the dark field area, divided by the total number of pixels in the dark field area, with no weighting applied. The rms in a given area is also be calculated from the dark-hole contrast field.

3.4. Milestone Demonstration Procedure

The procedure for the milestone demonstration is as follows:

3.4.1. The DM is set to scratch. An initial coronagraph contrast field image is obtained as described in Sec. 3.3.

3.4.2. Wavefront sensing and control is performed to find settings of the DM actuators that give the required high-contrast in the target dark field. This iterative procedure may take from one to several hours, starting from scratch, if no prior information is available. It can also take more or less time depending on the stability of the HCIT optical system.

3.4.3. A number of contrast field images are taken, following steps 3.3.1 – 3.3.2. The result is a set of contrast field images. It is required that a sufficient number of images are taken to provide statistical confidence that the milestone contrast levels have been achieved, as described in Section 3.1.7 above.

3.4.4. Laboratory data are archived for future reference, including raw and calibrated images of the reference star and contrast field images.

4. Success Criteria

The following are the required elements of the milestone demonstration. Each element includes a brief rationale.

4.1. Illumination is 10% percent light in single or dual polarization at a wavelength in the range of 400 nm $< \lambda <$ 900 nm.

Rationale: *This milestone is an initial demonstration of the feasibility of the approach at a wavelength in the science band of TPF-C or Exo-C.*

4.2. A mean contrast metric of 1 x 10^{-9} or smaller shall be achieved in a 3 to 8 λ/D dark zone, as defined in Sec. 3.3.2.

Rationale: *This provides evidence that the high contrast field is sufficiently dark (10^{-9} expected exozodi level) to be useful for searching planets, and to carry out initial tests at small angles.*

4.3. Criterion 4.2, averaged over the data set, shall be met with a confidence of 90% or better, as defined in Sec. 3.1.5. Sufficient data must be taken to justify this statistical confidence.

Rationale: *Assuming the contrast values have a Gaussian distribution about the mean contrast, this demonstrates a statistical confidence of 90% that the mean contrast goal has been reached.*

4.4. Elements 4.1 – 4.3 must be satisfied on three separate occasions with a reset of the wavefront control system software (DM set to scratch) between each demonstration.

Rationale: *This provides evidence of the repeatability of the contrast demonstration*.

The wavefront control system software reset between data sets ensures that the three data sets can be considered as independent and do not represent an unusually good configuration that cannot be reproduced. For each demonstration the DM will begin from a "scratch" setting. There is no time requirement for the demonstrations, other than the time required to meet the statistics stipulated in the success criteria. There is no required interval between demonstrations; subsequent demonstrations can begin as soon as prior demonstrations have ended. There is also no requirement to turn off power, open the vacuum tank, or delete data relevant for the calibration of the DM influence function.

5. Certification

The PI will assemble a milestone certification data package for review by the ExEPTAC and the ExEP program. In the event of a consensus determination that the success criteria have been met, the project will submit the findings of the review board, together with the certification data package, to NASA HQ for official certification of milestone compliance. In the event of a disagreement between the ExEP project and the ExEPTAC, NASA HQ will determine whether to accept the data package and certify compliance or request additional work.

5.1. Milestone Certification Data Package

The milestone certification data package will contain the following explanations, charts, and data products.

5.1.1. A narrative report, including a discussion of how each element of the milestone was met, and a narrative summary of the overall milestone achievement.

5.1.2. A description of the optical elements, including the vortex masks, and their significant characteristics.

5.1.3. A tabulation of the significant operating parameters of the apparatus.

5.1.4. A calibrated image of the reference star, and the photometry method used.

5.1.5. A calibrated image of the (distant) off-axis transmission of the vortex mask.

5.1.6. A contrast field image representative of the data set, with appropriate numerical contrast values indicated, with coordinate scales indicated in units of Airy distance (λ/ D).

5.1.7. For each image reported as part of the milestone demonstration, the average contrast recorded within the area spanning 3-4 λ/D.

5.1.8. A description of the data reduction algorithms, in sufficient detail to guide an independent analysis of the delivered data.

5.1.9. Contrast metric values and supporting statistics for the overall data used to satisfy the milestone requirements, including a pixel-by-pixel histogram of contrast values across the dark field.

6. Deviations from the Described Procedures

Note that as further work had been planned in order to push further toward the official milestone level, the demonstration runs used in this report were not actually planned to be milestone runs. As such, they do not conform exactly to all of the specifications mentioned above. Here the differences from the pre-specified goals and procedures are described.

In one of the three final runs, because of the wavefront-sensing approach involved, only three final null values are available instead of four. Nevertheless, the data over a longer time period are plotted to show the long-term trend.

The average contrasts obtained were slightly above the targeted milestone level, so the final contrasts are not “more than 3-sigma below the milestone level.” However, the contrast

level is less than 2 parts per billion, so within a factor of two of the planned milestone level, and as such, was deemed acceptable by the Exoplanet office.

7. Demonstration Results

The full dark hole wavefront sensing and correction process is described in detail in [21], so it is described only briefly here. For a given waveband, starting with a nominally flat surface figure setting on the DM for each run, we: (a) take a set of contrast field images with the initial DM setting; (b) take images for each of four "probe" DM settings (consisting of small deterministic surface figure deviations from the initial DM setting), (c) use these data to compute the complex electric field in the target dark field region (note that the 3 – 8 λ/D dark-hole region, called the "scoring" region, is selected in software from within the image of the field stop); and then (d) calculate and apply a new DM setting that will reduce the energy over the dark field, thus establishing a new "initial DM setting" in preparation for the next iteration, which is a loop back to step (a). For the milestone runs, because of low photon levels in the ultimate dark hole, integration times for individual dark hole images were 120 sec, and one complete wavefront sensing and control cycle, including overhead for CCD readouts, data handling and computations, thus took about 10 minutes. Figures 9-11 shows the contrast improvement as a function of iteration cycle (i.e., time) for several runs within three data sets, from which we selected the three best runs (gaps indicate the start of a new run). The contrast plotted is the ratio of dark hole level to the starlight level, as described earlier. Note that every five iterations the "beta-bumping" technique of Seo et al., in which the dark hole jumps to a worse value to avoid getting stuck in local minima, is applied.

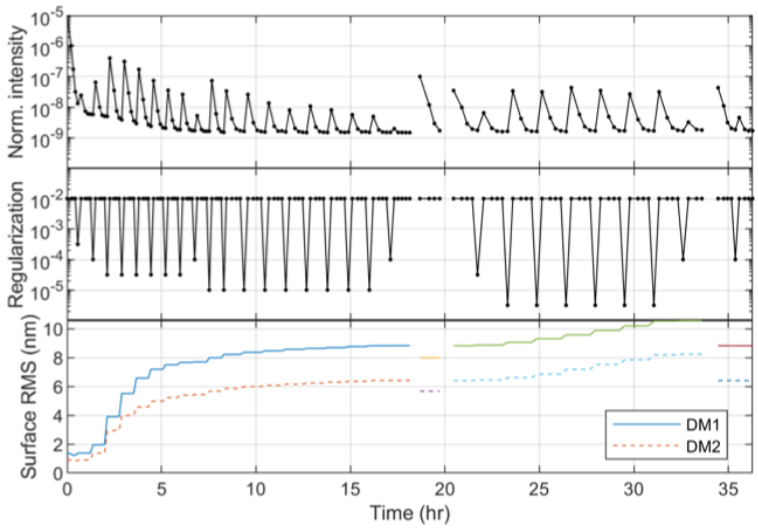

Fig. 9. *Contrast improvement in our dark hole during trials 15-18 on Dec 18-19, 2021*

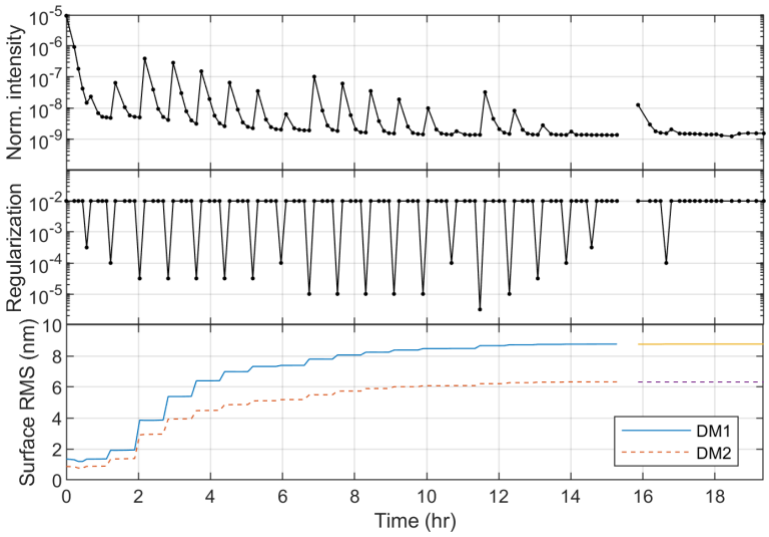

Fig. 10. *Contrast improvement in our dark hole during trials 19-20 on Dec 19-20, 2021.*

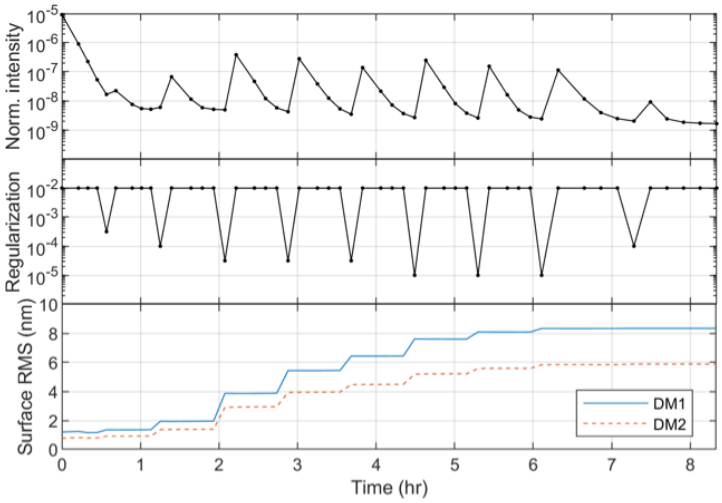

Fig. 11. *Contrast improvement in our dark hole during trial 26 on Dec 21, 2021*

Our three best runs within these data sets yielded the three mean normalized intensities shown in Table 3, in the dark zone defined over 3-8 λ/D. Averaging the data for the three dark holes in Table 3, we get an average contrast in the dark hole of $(1.83 \pm 0.12) \times 10^{-9}$. Our 1-σ confidence level is thus 1.95×10^{-9}, and our 3-σ confidence level is 2.2×10^{-9}. Our final dark hole, the average of all three dark hole runs, is shown in Fig. 12. The D-shaped dark-hole region in which the contrast is calculated is superposed on the Figure. The contrast over the full field shown is slightly better, i.e., 1.6×10^{-9} [21], because of the inclusion of even darker regions further from the star.

Table 3: Results summary for the final dark hole images in the three final runs

Attempt	Mean of final iterations	Sigma	Run notes
1	1.78e-9	0.01e-9	Used final 4 iterations of trial 15
2	1.63e-9	0.02e-9	Used final 4 iterations of trial 19
3	2.07e-9	0.12e-9	Used final 3 iterations of trial 26

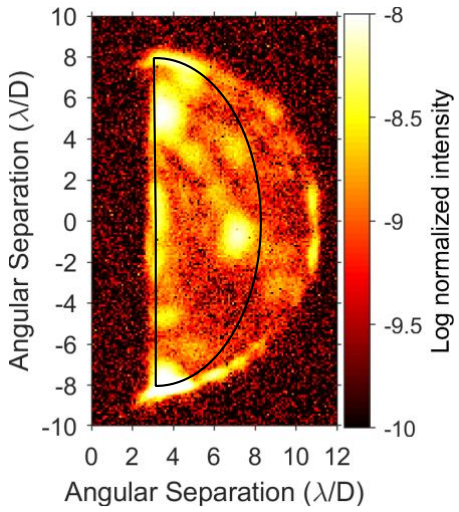

Figure 12. *Intensity in the full final dark-field region that is set by the size and shape of the field stop, averaged over all three runs. The black D-shaped outline superposed on the field shows the extent of the "scored" dark hole region used for the milestone calculations.*

As can be seen in Fig. 12, the main current limitation to reaching even deeper broadband contrasts is the presence of a few bright off-axis speckles. These bright speckles are persistent in location from iteration to iteration and run to run, and are well above photon and other statistical noise levels. Moreover, while they can be cancelled to a deeper level at a single wavelength, they cannot be cancelled effectively with broadband light. This is because they are found at fixed focal plane locations, which means that cancellation at different wavelengths would require different DM spatial frequencies. The suppression of these bright speckles therefore degrades with bandpass. To illustrate this effect; Fig. 13 shows dark hole contrast results (for a different test run) with our scoring dark hole region

set as the entire illuminated region of Fig. 12 (which extends along the x-axis roughly from 2.5 to 11 λ/D, and has a maximal extent in y of roughly ± 8 λ/D).

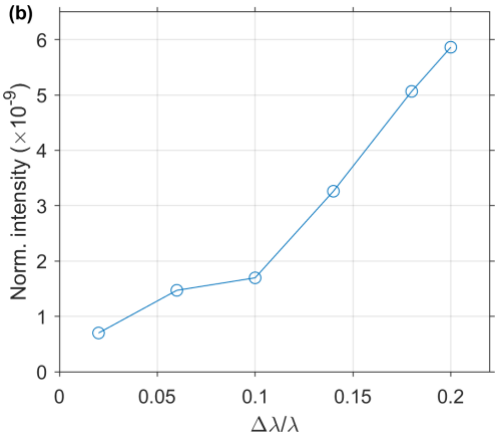

Figure 13. *Measured* 3 – 10 λ/D *dark-hole contrasts vs. radiation bandwidth*. [21]

While not completely understood, the bright speckles in Fig. 12 are thought to be due to small off-center mask imperfections or "defects" (e.g., Section 2.3) [21]. The exact nature of these defects is not unambiguously identified, but they are likely due to tiny inclusions in the mask's layered structure, e.g., either small dust particles trapped between individual layers. or small crystallization centers within individual liquid crystal polymer layers. Either of these would be at a specific focal-plane location, making it impossible to correct for their phase over a broad bandwidth by applying a sinusoid of a single spatial frequency to the DM, as each wavelength would require a sinusoid of a different spatial frequency. The absence of a central obscuring disk on the best-performing mask may also have some contributed extra light leakage, but, on the other hand, the excellent performance level reached without a central blocker in place is actually grounds for optimism.

8. Summary and Prospects

Using a vector vortex phase mask in the DST, an average contrast of $(1.83 \pm 0.12) \times 10^{-9}$ was obtained over a dark-hole extending from 3 – 8 λ/D, for single polarization light of 10% bandwidth centered at a 635 nm wavelength. As this is within a factor of 2 of the part per billion contrast level targeted in our milestone white paper, the exoplanet office has deemed this level acceptable for closing out work under TDEM award 14-SAT14-0008.

For broader context, it is also worth mentioning additional experiments that were carried out that go beyond the specific intent of our *14-SAT14-0008* milestone white paper. In particular, as mentioned, we have measured the mean dark-hole contrast attainable as a function of the radiation bandwidth. In that experiment, 2% sub-bands were added at each end of the wavelength range and a dark hole was again dug to re-optimize the DM solution to minimize the mean normalized intensity across the new wavelength range (until reaching 18% with nine sub-bands). We also did a 20% bandwidth case, again with nine sub-bands,

since future mission concepts have baselined 20% bandwidths. The results for a 3 – 10 λ/D dark hole are shown in Fig. 13 [21], where a steady rise in mean contrast with increasing bandwidth is seen: the contrast rises steadily from 7 x 10^{-10} for 2 % bandwidth light to 6 x 10^{-9} for 20% bandwidth light. Our narrow-band (2% bandwidth) performance is thus already below 10^{-9}, and our recent 4 x 10^{-10} laser result [21] over that same dark hole is even better, approaching our next TDEM (17-SAT17-0015) project's monochromatic milestone level of 3 x 10^{-10}. Moreover, the 20% bandwidth result suggests that more defect-free devices should enable quite broadband dark holes. Our next steps thus include an emphasis on the quality control of the masks to be produced, which should enable us to continue to push to deeper contrasts both for monochromatic and broadband light, and for both monolithic and segmented apertures. Our error budget analysis (Table 4) then indicates the next terms that will need to be addressed for further progress.

Table 4

Component	Error	Mitigation strategy	Contrast estimate
Deformable mirror	Quantization error	Next-gen DM electronics	~1e-10 for AOX + gen5 electronics
	Drift	Temperature control	Negligible.
Testbed	Tip/tilt jitter	Vibration isolation	Negligible.
	Circular analyzer	Procure the highest possible quality QWPs and LPs	~4e-10 with polarization filtering and monochromatic laser (637nm).
Vortex mask	Bulk retardance error (ε) (a.k.a on-axis leakage)	Minimized during FPM manufacture	
	Fine scale retardance error (amp. & phase)		~2e-10 (highly chromatic)
	Fast axis orientation error (phase)		~1e-10. To be confirmed. (highly chromatic)
	Local transmission errors		~2e-10. To be confirmed. (highly chromatic)
		Total:	**~1e-9**

This research was carried out at the Jet Propulsion Laboratory, California Institute of Technology, under a contract with the National Aeronautics and Space Administration (80NM0018D0004).

9. References

[1] https://exoplanets.nasa.gov/exep/studies/probe-scale-stdt/

[2] https://www.jpl.nasa.gov/habex/documents/

[3] https://asd.gsfc.nasa.gov/luvoir/reports/

[4] https://www.nationalacademies.org/our-work/decadal-survey-on-astronomy-and-astrophysics-2020-astro2020

[5] https://exoplanets.nasa.gov/exep/technology/TDEM-awards/

[6] Serabyn, E., Trauger, J., Moody, D., Mawet, D., Liewer, K., Krist, J., Kern, B., "High-contrast imaging results with the vortex coronagraph," *Proc. SPIE* **8864**, 88640Y-1, 2013.

[7] Guyon, O., Pluzhnik, E.A., Kuchner, M.J., Collins, B., and Ridgway, S.T., "Theoretical Limits On Extrasolar Terrestrial Planet Detection with Coronagraphs," *Ap.J. Suppl.* **167,** 81, 2006.

[8] Mawet, D. *et al.*, "Optical Vectorial Vortex Coronagraphs using Liquid Crystal Polymers: Theory, Manufacturing and Laboratory Demonstration," *Optics Express*, **17**, 1902, 2009.

[9] Serabyn E., D. Mawet & R. Burruss, "The potential of small space telescopes for exoplanet observations," *Proc. SPIE* **7731**, 77312O, 2010.

[10] Trauger, J. and W. Traub, "A laboratory demonstration of the capability to image an Earth-like extrasolar planet," *Nature* **446**, 771, 2007.

[11] Levine, M., Shaklan, S. & Kasting, J., "Terrestrial Planet Finder Coronagraph: Science and Technology Definition Team Report," JPL Publ. D-34923, 2006.

[12] Mawet, D., Riaud, P., Absil, O. & Surdej, J., "Annular Groove Phase Mask Coronagraph," *ApJ*, **633**, 1191, 2005.

[13] Swartzlander, G., "The optical vortex coronagraph, " *J. Opt. A.*, **11**, 1464, 2009.

[14] Serabyn, E. & Mawet, D., "Detecting Exoplanets with a Liquid-Crystal-Based Vortex Coronagraph," *Mol. Cryst. Liq. Cryst.* **559**, 69, 2012a.

[15] Mawet, D. *et al.*, "Taking the vector vortex coronagraph to the next level for ground- and space-based exoplanet imaging instruments: review of technology developments in the USA, Japan, and Europe," *Proc. SPIE* **8151**, 815108-1, 2011a.

[16] Pancharatnam, S., "Achromatic combination of birefringent waveplates," Proc. Indian Acad. Sci. A 41, 137, 1955.

[17] Komanduri, R. K. *et al.*, "Multi-twist retarders for broadband polarization transformation," Proc. SPIE 8279, 82790E (2012).

[18] Serabyn, E. *et al.*, "Vector vortex coronagraphy for exoplanet detection with spatially variant diffractive waveplates," JOSA B 36, D13

[19] Ruane, G. *et al.*, "Decadal Survey Testbed Commissioning Roadmap: Demonstrating Technology for Imaging New Worlds," 2019 https://exoplanets.nasa.gov/internal_resources/1170/

[20] Trauger, J. *et al.*, "ACCESS – A Concept Study for the Direct Imaging and Spectroscopy of Exoplanetary Systems," in "Pathways towards Habitable Planets," *ASP Conf. Ser.* **430**, 375, 2010

[21] Ruane, G. *et al.* (2022), "Broadband Vector Vortex Coronagraph Testing at NASA's High Contrast Imaging Testbed Facility, Proc. SPIE 12180, 1218024